JOURNAL OF AIRCRAFT
Vol. 46, No. 3, May–June 2009

# Sizing and Performance-Prediction Method for Rotary-Wing Ejector Nozzles

Alex M. Moodie,* Daniel P. Schrage,† and Lakshmi N. Sankar‡
*Georgia Institute of Technology, Atlanta, Georgia 30332*
and
Mark H. Waters§
*California Polytechnic State University, San Luis Obispo, California 93407*

DOI: 10.2514/1.39423

**A reaction-drive rotor configuration including an ejector nozzle is studied to determine possible exhaust-jet velocity reduction for the purpose of noise suppression. A vortex-wake rotor model is compared with an experimental rotor test, determining the model validity for a hovering rotor. A two-dimensional computational fluid dynamic model of an ejector flow is compared with an experimental ejector-nozzle test to determine the appropriate grid coarseness and turbulence model relevant to lift and drag predictions supporting the hovering-rotor aerodynamic model. The reaction-drive-rotor tip-jet-ejector nozzle geometry is sized by the analysis method put forward here, implementing coupled rotor aerodynamic, reaction-drive tip-jet-ejector thermodynamic, and computational fluid dynamic models. A performance version of the proposed analysis method is developed to characterize this rotor configuration over a range of blade collective pitch angles operating in a hovering-flight condition.**

## Nomenclature

| | | |
|---|---|---|
| $A$ | = | area |
| $C_d$ | = | drag coefficient |
| $C_l$ | = | lift coefficient |
| $C_P$ | = | power coefficient |
| $C_T$ | = | thrust coefficient |
| $D$ | = | duct diameter |
| $D_{\text{eq}}$ | = | equivalent circular diameter |
| $e$ | = | internal energy per unit mass |
| $FN$ | = | net thrust |
| $f_{\text{me}}$ | = | mixing effectiveness |
| GW | = | gross weight |
| $h_l$ | = | head loss |
| $h_{\text{lobe}}$ | = | lobed-nozzle lobe height |
| $h_S$ | = | lobed-nozzle flap separation |
| $i$ | = | iterate number |
| $l$ | = | length of the duct section |
| $\dot{m}$ | = | mass flow rate |
| $P$ | = | rotor power |
| $p$ | = | pressure |
| $p_N$ | = | lobed-nozzle perimeter |
| $Q$ | = | torque |
| $\dot{q}$ | = | heat rate per unit mass |
| $R$ | = | blade radius |
| $Re$ | = | Reynolds number |
| $R_{\text{lobe}}$ | = | lobed-nozzle lobe radius |
| $r$ | = | radial distance |
| $T$ | = | temperature, rotor thrust |
| $V$ | = | gas mean velocity |
| $W_N$ | = | lobed-nozzle width |
| $x$ | = | residual variable |
| $\Gamma$ | = | vortex filament strength |
| $\rho$ | = | density |
| $\Phi$ | = | thrust-augmentation ratio |
| $\Omega$ | = | rotor rotational speed |
| $\infty$ | = | ambient, freestream |

Received 27 June 2008; revision received 2 January 2009; accepted for publication 2 January 2009. 

*Graduate Research Assistant, Department of Aerospace Engineering, 270 Ferst Drive. Student Member AIAA.
†Professor, Department of Aerospace Engineering, 270 Ferst Drive. Fellow AIAA.
‡Professor, Department of Aerospace Engineering, 270 Ferst Drive. Associate Fellow AIAA.
§Lecturer, Aerospace Engineering, 1 Grand Avenue. Member AIAA.

## I. Introduction

SINCE the inception of the first practical rotorcraft in the early 20th century, there have been many variations explored to fulfill evolving requirements. Although the pure helicopter has proven to be a versatile machine in many respects, it still has limitations. The most notable limitation is the maximum forward airspeed due to compressibility effects and retreating blade stall resulting in high vibratory loads [1,2]. One possible solution to expand the main rotor limits is to compound the helicopter with a wing and auxiliary propulsion, offloading the rotor, and slowing the rotational speed, thereby increasing the forward-airspeed capabilities. Slowing the main rotor of a conventional transmission-driven helicopter requires multiple gear stages, increasing vehicle empty weight.

A reaction-drive rotor eliminates this problem by producing the required rotor torque with thrusters located at the blade tip. The rotor speed in forward flight may be controlled either by varying the thrust generated by the tip thrusters or by allowing the rotor to autorotate. There are two major types of reaction-drive systems: the pure tip-jet drive, in which the engine is mounted at the blade tip, and the pressure-jet drive, in which the engine is fixed to the fuselage and the tip-jet thrusters are apart of the propulsion exhaust [3]. There have been many flight-tested rotorcraft that have been powered by these systems: most notably, the Fairey Rotodyne, McDonnell XV-1, Hughes XV-9A, and, more recently, the X-50A Dragonfly canard rotor/wing. Although there have been many successful examples of this type of rotorcraft, none are currently in production. A major drawback to reaction-drive rotors compared with conventional helicopter rotors, other than lower overall efficiency, is the noise generated by the high-speed gas exhausting from the tip jet [4]. There are limited acoustic data available for prototype reaction-drive vehicles. However, takeoff acoustic data for the Hughes XV-9A Hot Cycle and Fairey Rotodyne are compared with the Sikorsky S-61 in Fig. 1, taken from [5]. The reaction-drive-rotor concepts generate

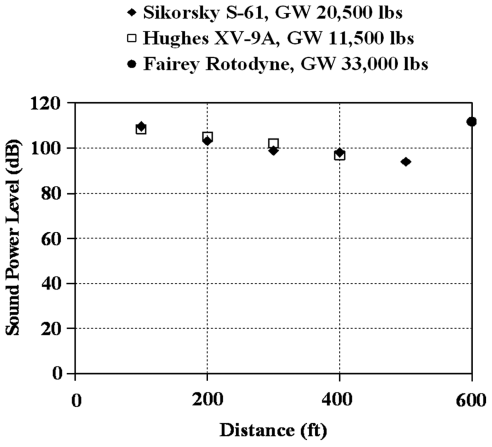


**Fig. 1 Vehicle noise comparison [5].**

significantly more noise when comparing their gross weights. The thrust produced by the tip-jet thruster and the associated noise are strongly dependent on the velocity of the gas exiting the thruster nozzle [3–7]. To maintain thrust and reduce the gas velocity, an additional gas flow needs to be entrained into the primary gas flow, trading mass for velocity while maintaining the fluid momentum. A possible solution is the addition of an ejector nozzle to the blade-tip thruster [8].

An ejector nozzle is a fluid pump in which a high-speed gas flow entrains a secondary flow into a mixing duct, reducing the exhaust velocity for a given thrust. These devices are simplistic in the sense that there are no moving parts required. However, they involve coupled fluid dynamic processes that complicate analysis and design. The ejector nozzle has been used for thrust and lift augmentation for vertical and short takeoff and landing vehicles, engine nacelle ventilation and exhaust cooling, and noise suppression [8–12].

## II. Model Formulation

### A. Rotor Aerodynamics

A blade element including a prescribed vortex-wake model based on Landgrebe's [13,14] work is used for this study. A general schematic of the wake generated by a hovering-rotor blade is presented in Fig. 2 [15]. The wake geometry is a function of the rotor geometry, including twist and taper, and thrust. Reference [2] contains a complete derivation of this prescribed vortex-wake approach to analytically model a hovering rotor.

The sectional lift and drag coefficients are compiled into tabular format as functions of Mach number and angle of attack. The rotor aerodynamic model can read different tables at any of the blade elements, allowing for more complex rotor planforms. Gas flow of high velocity and temperature is ejected from the tip region of a reaction-drive rotor into the surrounding flowfield. Previous research with jet flapped wings and jet wings has shown that a wing with jet exhausting from the trailing edge alters the pressure distribution and thus the lift and drag characteristics [16–18]. From this previous work, computational fluid dynamics (CFD) appears to be the minimum level of analysis fidelity to compute the required airloads needed for this type of rotor problem. To capture the three-dimensional effects inherently present for a hovering rotor and any interactions with the tip-jet-ejector exhaust flow requires a large number of computational-grid points to adequately model the flow around this complicated geometric configuration. This would place a significant computational cost on the modeling effort; therefore, two-dimensional CFD models are used to generate the sectional airloads at the tip region.

### B. Reaction-Drive Rotor Thermodynamics

To achieve a trimmed flight condition for a reaction-drive rotor, the jet thrust produced at the tip multiplied by the rotor radius and the number of blades must equal the torque generated by the rotor to produce a given amount of rotor thrust. This additional degree of freedom in the trim procedure requires a thermodynamic analysis to determine the pressure, temperature, and Mach number at the exit plane of the primary nozzle based on a compressed-air source. The flow conditions computed using the thermodynamic model are then supplied to the two-dimensional CFD model as boundary conditions for the high-speed nozzle flow.

The reaction-drive rotor is analogous to a turbine, in which compressed gas is expanded to produce work. In this case, compressed gas travels up a fixed duct, transitioning to a rotating duct, then turned 90 deg into a rotating duct. The gas travels to the end of the rotating duct, turns 90 deg again, and is mixed with fuel, combusted, and expanded through a nozzle to the atmosphere. The basic operation of a reaction-drive rotor is presented in Fig. 3. Reaction-drive rotor systems may be subdivided into several components: rotor-head supply duct, blade duct, combustion chamber, and converging-diverging nozzle.

The rotor-head supply duct provides the flowpath from the gas source to the rotor hub. There may be varying cross-sectional areas and shapes, baffles, turns, and other geometric features dictated by the layout of the engines, airframe, and rotor. Relationships for the frictional losses for these types of duct configurations applied to reaction-drive rotors have been investigated by [19–21]. The pressure drop due to the frictional losses, or head loss, for turbulent duct flow is given in [22]. The friction factor can be found in the work of [23] and empirically corrected for curved-duct sections relating the duct $l/D$ to $r/D$ [22].

The duct inside the blade delivers air from the rotor head to the blade tip. The first law of thermodynamics can be applied to the control volume in a rotating reference frame, resulting in

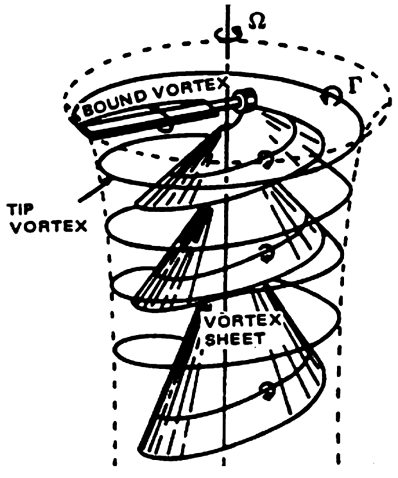


**Fig. 2 Notional wake structure for single blade in hover [15].**

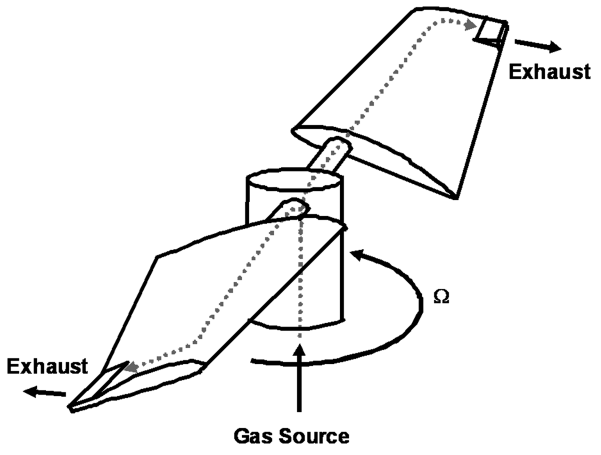


**Fig. 3 Reaction-drive-rotor schematic.**

$$\dot{q} = \int_{CS} \left[ \rho \left( \frac{e + V^2 + (\Omega r)^2}{2} \right) + p \right] \mathbf{V} \cdot \mathrm{d}\mathbf{A} \tag{1}$$

where $(\Omega r)^2/2$ is the kinetic energy added to the fluid due to the rotation, typically referred to as centrifugal pumping. Assuming the flow is adiabatic, incompressible, and fully developed, the continuity relation and Eq. (1) applied to the rotating control volume in Fig. 4 give the following relation:

$$0 = \Omega^2 (r_2^2 - r_1^2)/2 + (p_2 - p_1)/\rho - h_l \tag{2}$$

The gas flow at the end of the rotating duct inside the rotor blade can be mixed with fuel and combusted or simply expanded through a nozzle, depending on the configuration. One advantage to burning additional fuel at the blade tip is that the increase in thermal energy results in a lower gas-flow requirement for a given nozzle thrust, reducing the diameter of the blade duct and associated rotor solidity. The thrust produced by expanding the gas through a nozzle is given by

$$FN = \dot{m}(V_{\text{jet}} - \Omega R) \tag{3}$$

where $-\dot{m}\Omega R$ is the force imparted on the rotor at the nozzle radial location due to the acceleration of the gas transitioning from the body reference frame to the blade rotating reference frame as it is ducted down the blade to the tip.

### C. Ejector-Nozzle Thermodynamics

Considering an ejector nozzle integrated with the tip jet includes additional variables associated with the ejector-nozzle geometry (cross-sectional areas and length) and flow conditions (temperature, pressure, Mach number, etc.). A basic schematic of an ideal ejector nozzle assuming constant area mixing is presented in Fig. 5. Ejector nozzles are typically composed of two physical components: a primary nozzle and a duct or shroud. A quasi-one-dimensional thermodynamic representation of this system is subdivided into three components: secondary inlets, primary nozzle, and ejector-exit nozzle.

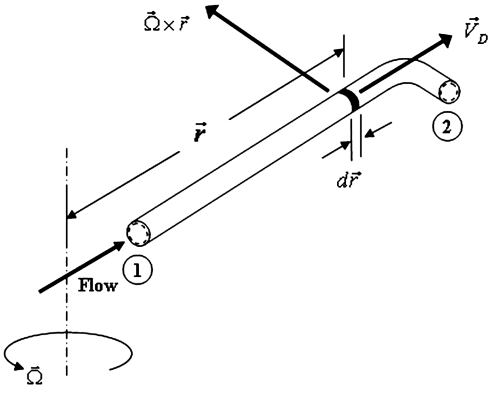


**Fig. 4 Schematic of a rotating duct.**

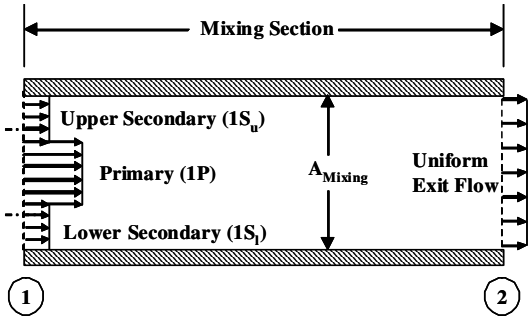


**Fig. 5 Ideal ejector control volume.**

The secondary inlets provide a flowpath from the freestream to the mixing plane and, for this study, diffuse the flow to a specified velocity. The primary nozzle is assumed to be either convergent or convergent–divergent, depending on the nozzle-exit Mach number. The ejector-exit gas flow will be a sum of primary and secondary gas flows represented by the following form of the continuity equation:

$$\dot{m}_{1P} + \dot{m}_{1Su} + \dot{m}_{1Sl} = \dot{m}_2 \tag{4}$$

The subscripts $u$ and $l$ denote the upper and lower secondary flows, which are assumed to be asymmetric for this ejector application. Similarly, the momentum through the control volume in Fig. 5, assuming steady-state, quasi-one-dimensional, and ideal gas, reduces to the following relation:

$$[(\dot{m}V + p)A]_{1Su} + [(\dot{m}V + p)A]_{1Sl} + [(\dot{m}V + p)A]_{1P} = [(\dot{m}V + p)A]_2 \tag{5}$$

Conservation of energy applied to the control volume, assuming adiabatic flow in addition to the assumptions listed for Eq. (5), gives

$$[(\rho(e + V^2/2) + p)VA]_{1Su} + [(\rho(e + V^2/2) + p)VA]_{1Sl} + [(\rho(e + V^2/2) + p)VA]_{1P} = [(\rho(e + V^2/2) + p)VA]_2 \tag{6}$$

Equations (4–6) represent a system of three equations with the ejector-exit Mach number, ejector-exit pressure, and secondary-inlet mass flow rate as the three unknowns.

A major assumption is that the secondary and primary flows are fully mixed at the ejector exit. This assumption is necessary to close Eqs. (4–6) for the control volume shown in Fig. 5. The reality of this problem is that there will not be sufficient length to completely mix the primary and secondary flows. A forced-mixing nozzle is one option to increase the mixing between the primary and secondary gas flows, shown in Fig. 6. An empirical relationship for a lobed forced-mixing nozzle relating the partially mixed thrust to the fully mixed and unmixed ideal thrust, taken from [24], is given by

$$FN_{\text{jet,par mix}} = f_{\text{me}}(FN_{\text{jet,full mix}} - FN_{\text{jet,unmix}}) + FN_{\text{jet,unmix}} \tag{7}$$

The mixing effectiveness is empirically related to the primary-nozzle geometry and ejector shroud length and is presented in Fig. 7. The lobed forced-mixing nozzle perimeter is determined by

$$p_N = 4N_{\text{lobe}}(\pi R_{\text{lobe}} + (h_{\text{lobe}} - 2R_{\text{lobe}})) + h_S \tag{8}$$

The equivalent circular diameter of the lobed forced-mixing nozzle is calculated by

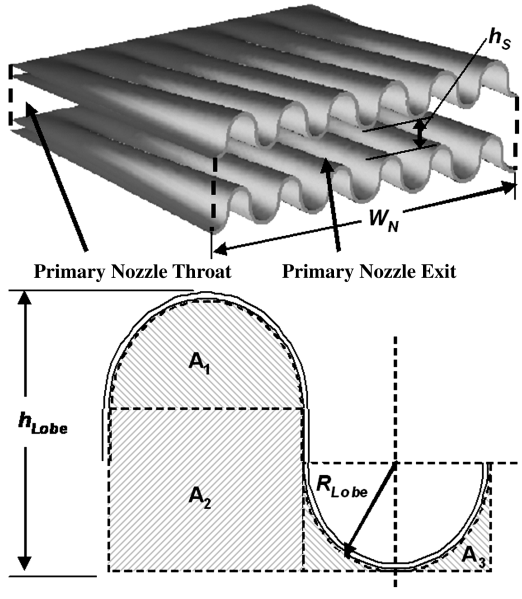


**Fig. 6 Lobed forced-mixing nozzle.**

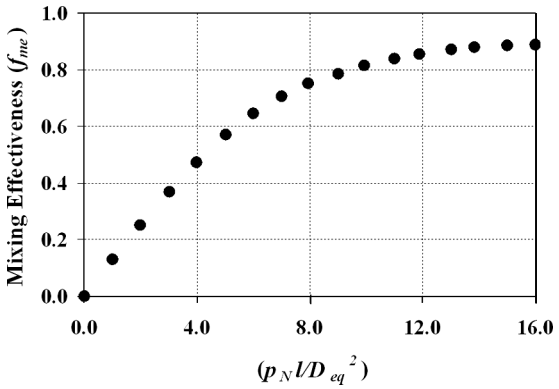


**Fig. 7 Mixing effectiveness [24].**

$$D_{\text{eq}} = [4(2N_{\text{lobe}}(A_1 + A_2 + A_3) + h_S W_N)/\pi]^{1/2} \qquad (9)$$

### D. Computational Fluid Dynamics

The analysis of the reaction-drive tip-jet-ejector rotor relies on the prediction of the two-dimensional sectional lift and drag of the blade. The CFD tool used in this study is CFL3D, a Reynolds-averaged thin-layer Navier–Stokes multiblock flow solver for structured grids with parallel processing capabilities. A semidiscrete finite volume approach is used for spatial discretization, upwind biasing for convective and pressure terms, central differencing for shear stress, and implicit time advancement for steady and unsteady flows, including a handful of turbulence models ranging from zero-equation to two-equation [25]. Multigrid convergence acceleration is also available, including *V*-cycle and *W*-cycle formulations, requiring grid dimensions such that when every other grid point is removed, the dimensions still maintain an integer value.

The structured grids are generated using Gridgen® [26,27]. For high-Reynolds-number flows, the viscous effects are predominately confined near surfaces and in the body wakes, including tip vortices. The thin-layer approximation allows for the grid points to be concentrated in the normal direction to the surfaces, greatly reducing the computational time. CFL3D is a multiblock solver; therefore, the grid may be split into many smaller grids to take advantage of parallel processing, further reducing computational time.

A Richardson extrapolation is implemented to determine if the grid is fine enough for the problem at hand [28]. Three grid-coarseness levels are required to estimate the solution at the zero-grid spacing and estimate the error associated with the CFD predictions. The grid convergence is achieved when the solution asymptotically approaches the zero-grid solution through refining the grid coarseness. Using the multigrid feature within CFL3D allows for a grid convergence study using one grid. The global drag is used as the metric to determine grid convergence and is therefore reported at each grid-coarseness level. A derivation of the procedure to determine the grid convergence and model error is described in [29].

### E. Tip-Jet-Ejector Sizing Method

The first step in predicting the performance of a tip-jet ejector nozzle integrated with a reaction-drive rotor is to size the ejector geometry based on a given rotor configuration. This requires the integration of the rotor aerodynamic model, reaction-drive thermodynamic model, ejector thermodynamic model, and two-dimensional CFD model. A basic ejector layout is selected for this study, with upper and lower shrouds trailing aft of the blade tip, as shown in Fig. 8. The two-dimensional geometric configuration of this ejector nozzle allows for a computational grid divided into three primary blocks: an inner and outer *C*-grid and an exhaust grid. The geometric definition of this blade section is based on a NACA 0012 airfoil. To determine the upper and lower inlet areas, mixing section area, and exit area of the ejector nozzle, both the chordwise position and length of the ejector are assumed. In addition, the chordwise

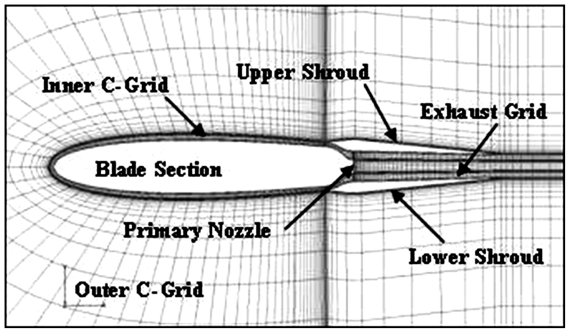


**Fig. 8 Tip-jet-ejector nozzle layout.**

length of the ejector inlets and width of the ejector nozzle in the rotor blade radial direction are assumed to be known. The three-dimensional effects of the forced-mixing nozzle, shown in Fig. 6, and the nozzle radial end plates are neglected in the two-dimensional CFD model. The primary nozzle is replaced with an equivalent-area rectangular nozzle, allowing for symmetry in the radial direction, thereby reducing dimensionality.

To begin the sizing procedure for this ejector nozzle, a first guess of the lift, drag, upper and lower inlet pressures, temperature, and Mach number are required. As an initial starting point, the sectional lift and drag coefficients are taken from the clean unmodified blade airfoil. The secondary-inlet pressure, temperature, and Mach number are initially equal to the freestream conditions at the rotor blade tip. The lift and drag of the blade-tip section are used in the rotor aerodynamic model to predict the required torque to hover and subsequent tip-jet-ejector thrust. The reaction-drive and ejector-nozzle thermodynamic models balance the flow conditions and areas needed to produce the required thrust. With the tip-jet-ejector nozzle geometry defined, a computational grid can be generated. CFL3D is used to compute the lift and drag over a range of angles of attack and freestream Mach numbers. Data collected from the CFD model sweeps provide updated sectional lift and drag coefficients for the rotor aerodynamic model and the upper and lower inlet flow conditions for the ejector-nozzle thermodynamic model. After the ejector solution has been updated, it is compared with the previous solution to determine the relative change in ejector geometry and flow conditions, which are metrics for convergence. A graphical representation of the tip-jet-ejector sizing method is presented in Fig. 9.

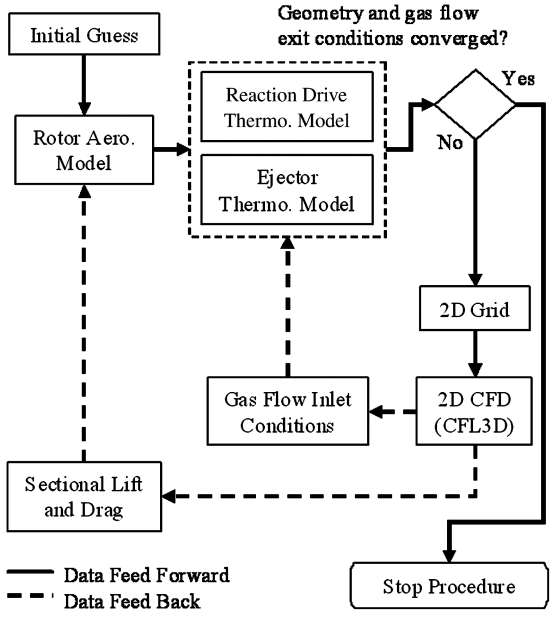


**Fig. 9 Tip-jet-ejector sizing-procedure flowchart.**

### F. Tip-Jet-Ejector Performance-Prediction Method

Offdesign reaction-drive and ejector-nozzle thermodynamic models have been developed to predict the performance for a range of hovering- and forward-flight conditions. The current study is focused on a hovering-rotor model; however, forward flight could be analyzed by simply replacing the rotor aerodynamic model and computing the tip-jet-ejector sectional lift and drag over a broader range of angles of attack and Mach numbers. The use of CFL3D is similar to the tip-jet-ejector sizing procedure, computing the sectional lift and drag and the secondary-inlet temperature, pressure, Mach number, and mass flow as a function of angle of attack, freestream Mach number, and primary-nozzle flow conditions.

The hovering-rotor model computes the required torque for given rotor collective pitch angles, using the CFD-generated data. The torque required is then passed to the reaction-drive and ejector offdesign thermodynamic models. The primary-nozzle and ejector-exit areas are then used to update the two-dimensional computational grid used by CFL3D to update sectional airloads and the secondary-inlet conditions. This procedure is iterated until the change in the ejector-nozzle exit area and primary-nozzle flow conditions for each blade collective pitch has reached a given set of convergence criteria. The tip-jet-ejector performance-prediction method allows for varying rotor thrusts and flight conditions. A graphical representation of the tip-jet-ejector rotor-performance-analysis method described is presented in Fig. 10.

## III. Results and Discussion

### A. Rotor Model Validation

The rotor selected for this study is based on the configuration tested by [30]. The lift coefficient was computed from pressure measurements taken in the radial and chordwise directions along the rotor blade surface, serving as the primary metric for comparison. The rotor parameters taken from [30] are presented in Table 1. The rotor thrust and power, in coefficient form, are given using

$$C_T = T/\rho A(\Omega R)^2, \qquad C_P = P/\rho A(\Omega R)^3 \tag{10}$$

A comparison between the experiment and the blade-element prescribed vortex-wake model is presented in Table 2. The experimental value for the rotor power required was not available in [30]. However, [31] analytically computed the power coefficient, which is tabulated for comparative purposes. The radial load distribution provides a good benchmark for comparison and is shown in Fig. 11, in which it is clear that the rotor model is capturing the nonuniform trend in the radial load distribution. The blade-element prescribed vortex-wake model used for this study shows a good overall agreement with the data available in [30].

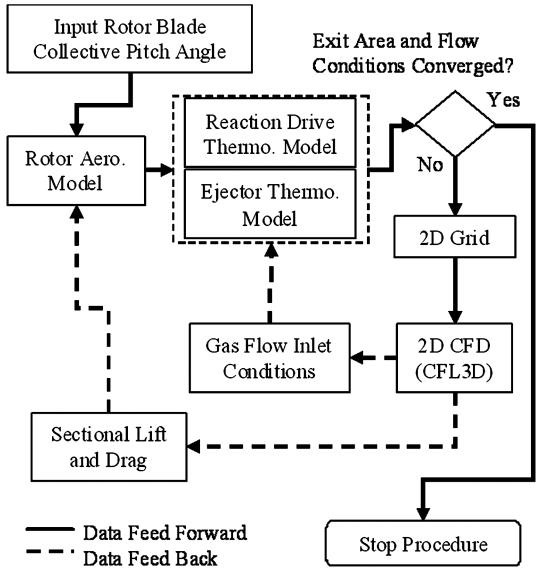


Fig. 10 Tip-jet-ejector rotor-performance-analysis flowchart.

Table 1 Rotor parameters

| | |
|---|---|
| Radius, ft | 3.75 |
| Mean chord, ft | 0.5 |
| Root cutout, ft | 0.75 |
| Number of blades | 2 |
| Rotor rpm | 1250 |
| Tip speed, ft/s | 491 |
| Collective pitch angle, deg | 12 |

Table 2 Thrust and power comparison

| | $C_T$ | $C_P$ |
|---|---|---|
| Experiment [30] | 7.90E − 3 | —— |
| Prediction [31] | 8.30E − 3 | 0.958E − 3 |
| Vortex-wake model | 7.84E − 3 | 0.830E − 3 |
| Error, % | 0.77 | —— |

Table 3 Two-dimensional ejector boundary conditions

| | $p/p_\infty$ | $T/T_\infty$ | $p_\infty$, lb/ft$^2$ | $T_\infty$, R |
|---|---|---|---|---|
| Secondary inlet | 1.00 | 1.00 | 2131.20 | 547.00 |
| Primary nozzle | 2.42 | 1.19 | 2131.20 | 547.00 |
| Outlet | 1.06 | 1.00 | 2131.20 | 547.00 |

### B. CFD Model Verification

The ejector experiment selected to correlate the two-dimensional CFD model was conducted by [32]. The ejector configuration includes a high-aspect-ratio rectangular nozzle enclosed by a duct with a bell-mouth inlet and exhaust diffuser. This experimental ejector study was selected because of the large volume of data available, especially the mixing section traverse data, in which the primary mechanism for the mixing of the high- and low-speed flows is through the turbulent shear layer. Turbulent mixing in an inherently unsteady process; however, the data recorded in the experiment only include the mean flow components. Therefore, the flow is assumed to be steady, further simplifying the problem. Several turbulence models are applied to determine which is appropriate, including $k$-$\varepsilon$, Spalart–Allmaras, $k$-$\omega$, and Menter's $k$-$\omega$ shear stress transport (SST).

The computational grid is presented in Fig. 12, with every fourth point shown for clarity. The grid contains 93,144 points, with 60,258 points used for the mixing section. The grid is split into four blocks. The first two blocks are the upper and lower inlet sections up to the primary-nozzle exhaust. The third block is the convergent primary nozzle, and the fourth block contains the mixing section. Each block

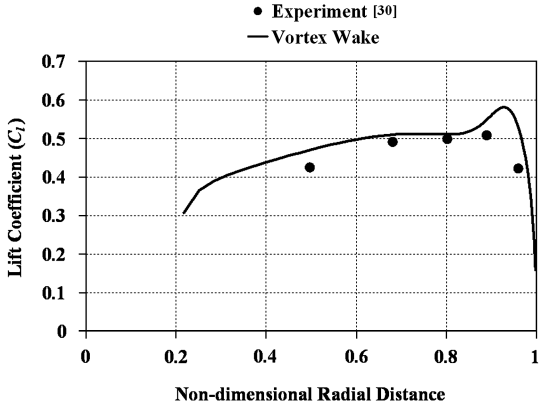


Fig. 11 Radial lift coefficient distribution.

**Table 4 Ejector mass-flow-rate comparison**

| | Mass flow rate, lb/s | | |
|---|---|---|---|
| | Inlet | Nozzle | Outlet |
| Experiment [32] | 2.77 | 0.71 | 3.47 |
| Coarse grid | 3.17 | 0.72 | 3.89 |
| Medium grid | 2.74 | 0.72 | 3.45 |
| Fine grid | 2.74 | 0.72 | 3.45 |
| Richardson extrapolation | 2.74 | 0.72 | 3.45 |
| Error, % | 0.85 | −1.42 | 0.52 |

is multigridable to four coarseness levels to accelerate convergence. Additionally, the blocks are split into smaller equal-sized blocks to take advantage of parallel processing.

The high-speed flow exhausting from the nozzle will draw the ambient air into the ejector. This fluid entrainment results in a positive flow at the entrance of the bell mouth. The boundary condition at this location is assumed to be an inflow. The ejector-exhaust pressure ratio is subsequently adjusted to match the measured mass flow rate. The shroud walls are assumed to be adiabatic with the no-slip condition. The flow boundary conditions for this model are summarized in the Table 3.

The data used for correlation purposes from [32] include mass flow rates, velocity traverse data, and the shroud wall pressure. Grid convergence for this model is determined by comparing the mass flow rates for varying grid-coarseness levels and is presented in Table 4 using the Spalart–Allmaras turbulence model. Table 4 shows a very good agreement between the ejector mass flow rates, indicating that the fluid-entrainment process is captured. Both the extrapolated and fine-grid mass flow rates are within $+1.5\%$ of the experimental values, indicating good grid convergence. The estimated uncertainty in the experimental value of the exit mass-flow-rate calculation is $\pm 4\%$ [32]. The error computed in Table 4 is well within that range. The calculated error in the mass flow rate of the primary nozzle was at least $\pm 1\%$, with an estimated increase in nozzle area of 0.33% when pressurized [32]. The error in the primary mass flow rate between the experimental value and CFD value is slightly over experimental error.

The experimental velocity-profile data were calculated through the isentropic relations for compressible flows from the measured static and stagnation pressures and the stagnation temperature. Because the mass flow rate is computed from the traverse data, the associated uncertainty is assumed to be derived directly from the transverse data measurements [32]. For brevity, the velocity-profile comparisons are only shown for two traverse positions downstream of the nozzle: 3 and 10.5 in. It is apparent from Figs. 13 and 14 that the velocity-profile trends are captured. Menter's $k$-$\omega$ SST and Spalart–Allmaras both show good agreement with the experimental data. Abid's $k$-$\varepsilon$ underpredicts the mixing between the high- and low-speed flows, indicated by the increased peak and reduced spread of the velocity profile. Wilcox's $k$-$\omega$, on the other hand, overpredicts the mixing compared with the experimental data, indicated by the reduction in the peak velocity and the increased spread of the profile. The static pressure was measured through pressure ports at various locations downstream of the nozzle. There is only a small error

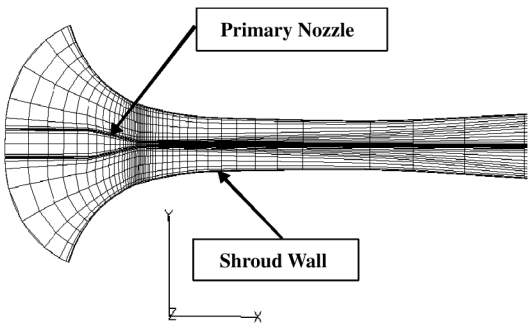


**Fig. 12 Two-dimensional ejector grid.**

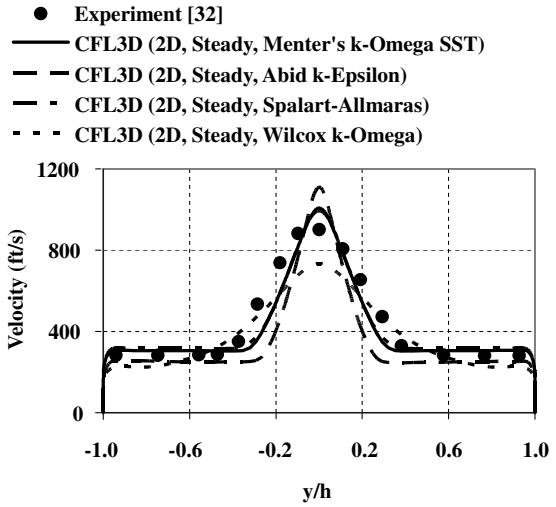


**Fig. 13 Velocity profile 3 in. downstream of nozzle.**

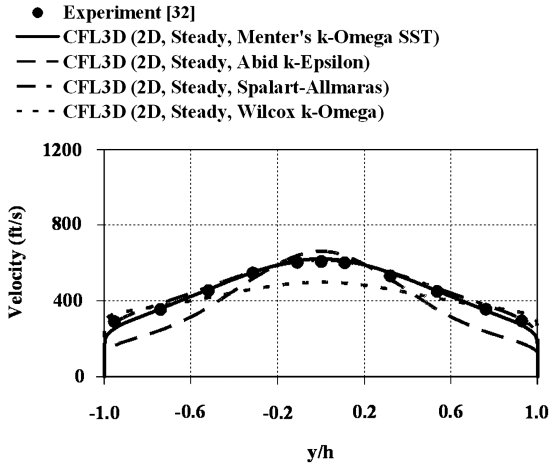


**Fig. 14 Velocity profile 10.5 in. downstream of nozzle.**

associated with this experimental data, amounting to approximately 0.4% [32]. Figure 15 shows a good agreement of the wall static pressure between the experiment and the two-dimensional CFD models.

Overall, the CFD model of this ejector shows promising results. Based on the results, the Spalart–Allmaras and Menter's $k$-$\omega$ SST

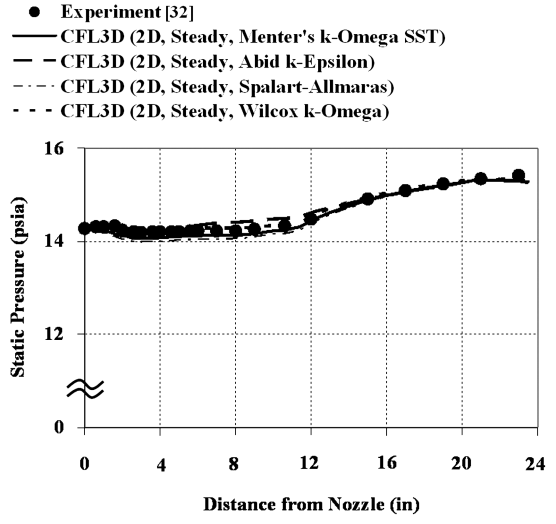


**Fig. 15 Shroud wall static pressure.**

turbulence models give a better overall prediction of the two-dimensional ejector flow. Spalart–Allmaras is a one-equation turbulence model, whereas Menter's $k$-$\omega$ SST is a two-equation turbulence model. Spalart–Allmaras requires the least computer resources between the two turbulence models and is selected for all of the subsequent two-dimensional CFD modeling.

### C. Tip-Jet-Ejector Sizing

The tip-jet-ejector sizing procedure begins with the basic rotor parameters presented in Table 1 and sectional lift and drag values obtained from [33] for a NACA 0012 airfoil. The subsequent sizing iterations rely on the lift and drag predicted using two-dimensional CFD modeling on the geometric configuration presented in Fig. 8 for the tip-jet-ejector section of the blade. Overall convergence is determined both geometrically and thermodynamically through the change in flow areas and flow parameters within the ejector nozzle.

The two-dimensional structured grid generated for the rotor blade tip-jet-ejector section, shown in Fig. 8 with every fourth point displayed for clarity, contains 841,854 points and is multigridable to four grid-coarseness levels. Only the final three grid-coarseness levels are used to determine grid convergence. There are a total of 33 two-dimensional CFD models run for each iteration, representing 8 angles of attack ranging from 0 to 14 deg and 3 Mach numbers ranging from 0.3 to 0.5. For brevity, a sample of these models is selected to examine the two-dimensional CFD model grid convergence using the drag coefficient as a metric, presented in Fig. 16.

Geometric convergence of the tip-jet-ejector sizing procedure is determined by the change in the upper and lower inlet and ejector-exit areas relative to the previous iteration and is generally defined by

$$\text{residual} = \left[\sum_{j}\left(\frac{x_{j,i+1} - x_{j,i}}{x_{j,i}}\right)^2\right]^{1/2} \tag{11}$$

The convergence criterion for the ejector geometry is $10^{-3}$, which was achieved after 10 iterations, as shown in Fig. 17. The ejector flow convergence history of the tip-jet-ejector sizing procedure is composed of the residuals of continuity, momentum, energy, and their respective sum. The resulting convergence history for the ejector exhaust flow after 10 iterations is presented in Fig. 18. The convergence criterion represents less than 0.005/in.$^2$ in area, 1°R, and 0.0001/lb of air per second. More stringent convergence can be achieved by increasing the number of iterations before convergence. The current procedure requires a manual grid generation for each step, prohibiting the full automation and increasing the overall workload of the sizing procedure.

The sized-ejector nozzle for the rotor described in Table 1 is presented in Table 5. The trust-augmentation ratio is a performance metric for ejector nozzles and is defined by

$$\Phi = FN_{\text{ejector}}/FN_{\text{primary nozzle}} \tag{12}$$

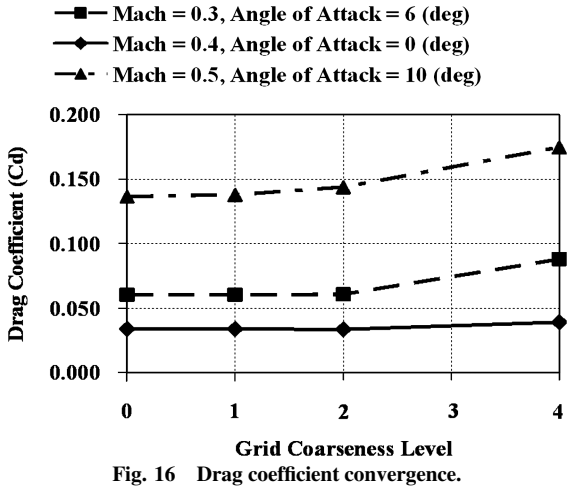


**Fig. 16 Drag coefficient convergence.**

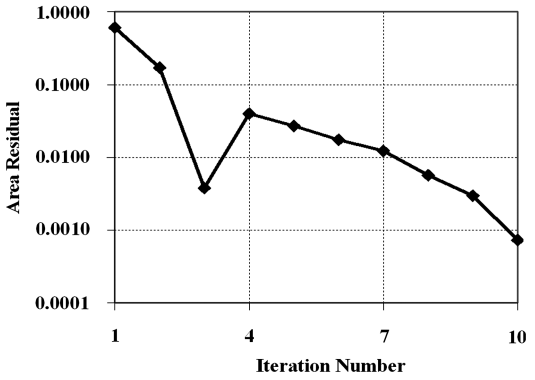


**Fig. 17 Geometric convergence history.**

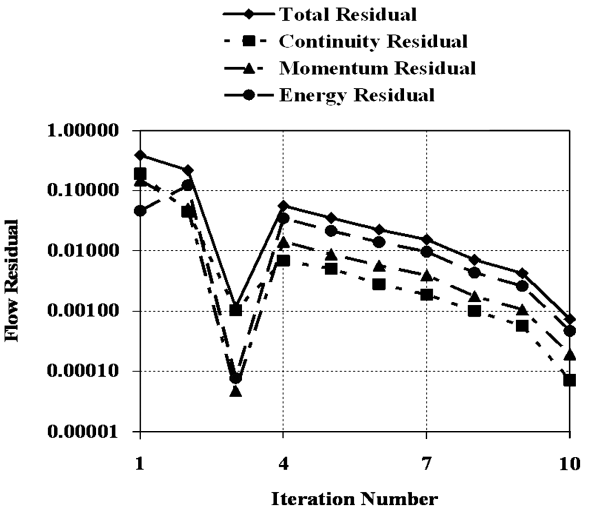


**Fig. 18 Ejector flow residual.**

The thrust-augmentation ratio indicates the amount of energy transferred from the primary-nozzle thrust generation to the ejector fluid entrainment. The ejector nozzle is traveling through the air at approximately Mach 0.4. The forward-speed effect tends to reduce the thrust-augmentation ratio, primarily due to ram drag [34]. The reduction in thrust generated by the ejector nozzle due to this transfer of energy requires the addition of energy from the primary nozzle (in this case, additional fuel) to meet the tip-jet-ejector thrust requirement of the hovering rotor.

A comparison of the radial load distribution is presented in Fig. 19. The tip-jet-ejector rotor shows a reduced amount of lift along the

**Table 5 Sized-ejector parameters**

| | |
|---|---|
| *Ejector geometry* | |
| Upper secondary-inlet area, in.$^2$ | 0.37 |
| Lower secondary-inlet area, in.$^2$ | 0.35 |
| Primary-nozzle area, in.$^2$ | 0.83 |
| Exit area, in.$^2$ | 1.79 |
| Mixing section $L/D_e$ | 1.22 |
| *Ejector flow parameters* | |
| Primary-nozzle mass flow rate, lb/s | 0.31 |
| Upper secondary mass flow rate, lb/s | 0.09 |
| Lower secondary mass flow rate, lb/s | 0.09 |
| Total mass flow rate, lb/s | 0.49 |
| Exit Mach number | 0.70 |
| Exit velocity, ft/s | 1165.33 |
| Exit stagnation temperature, R | 1282.88 |
| Ejector-nozzle thrust, lb | 21.40 |
| Thrust-augmentation ratio, Φ | 0.97 |
| *Rotor and tip-jet parameters* | |
| Power required, hp | 18.00 |
| Blade collective pitch angle, deg | 12.00 |
| Fuel flow: jet propellant 8, gal/h | 4.69 |

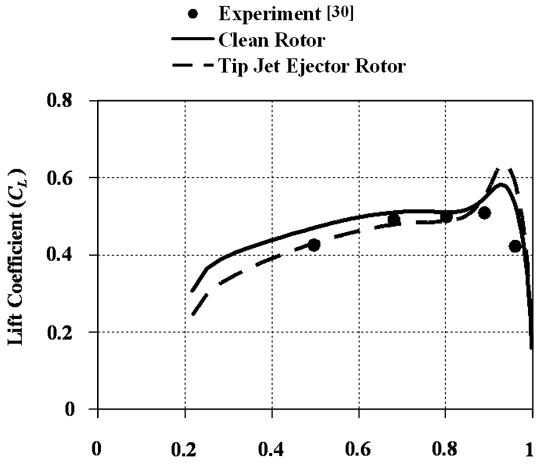


**Fig. 19 Radial lift coefficient distribution.**

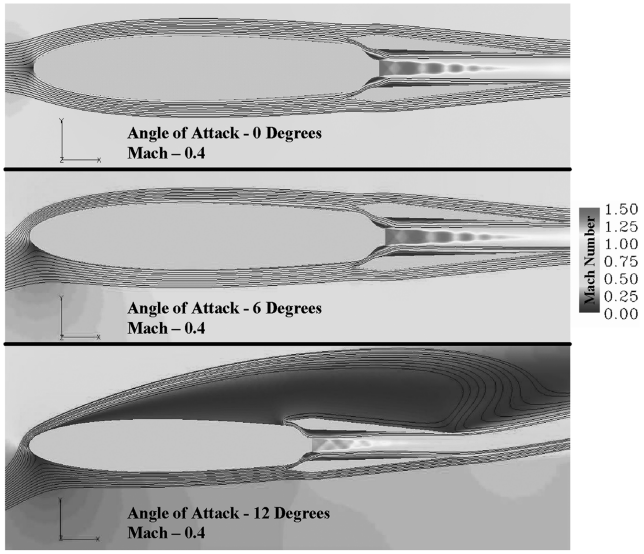


**Fig. 21 Two-dimensional CFD flow visualization.**

majority of the blade, with a pronounced increase at the tip region. It is difficult to determine whether this behavior is physical or may be the result of the rotor aerodynamic model. The increased lift at the tip region increases the strength of the tip vortex filament, which results in a greater contribution to the downward vertical component of the velocity vector at each blade element. An increase in the downward velocity, or inflow, reduces the local angle of attack and, therefore, the lift produced by the respective blade element.

The increased drag of the tip-jet-ejector nozzle blade section, shown in Fig. 20, is expected due to the geometry and jet exhaust. The maximum lift coefficient is slightly greater for the tip-jet-ejector element. A closer inspection of the CFD results shows some recirculation of the airfoil upper surface separated flow into the upper inlet at the higher angles of attack, shown in Fig. 21. Figure 22 shows that the local angle of attack of the tip-jet-ejector section of the rotor blade is not greater than 5 deg, which is well below the flow-separation condition due to stall. The discontinuous break in the radial distribution of the local angle of attack indicates the change from the NACA 0012 airfoil section to the tip-jet-ejector section within the rotor aerodynamic model. A comparison of the thrust and power between the tip-jet-ejector rotor and clean rotor is presented in Table 6. The resulting rotor thrust coefficient is significantly less for the same collective pitch angle and has a higher power requirement. Trimming the blade collective pitch angle to match the rotor thrust will further increase the power required above the baseline rotor configuration, as shown in Table 6.

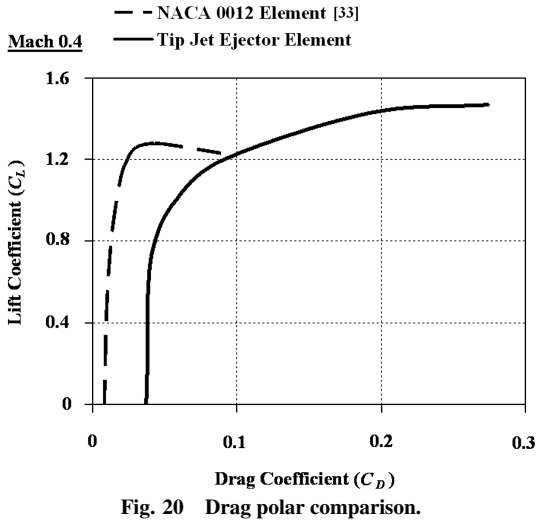


**Fig. 20 Drag polar comparison.**

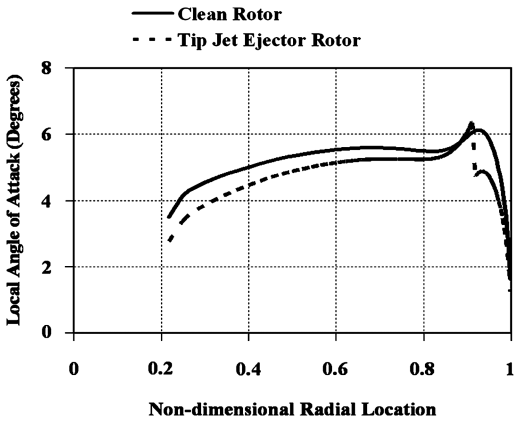


**Fig. 22 Radial distribution of angle of attack.**

### D. Tip-Jet-Ejector Performance

The tip-jet-ejector performance analysis, shown in Fig. 10, is applied to a range of rotor blade collective pitch angles from 8 to 14 deg. At each collective pitch angle, the primary-nozzle flow conditions are computed based on the rotor aerodynamic model, which is dependent on the blade-tip CFD-predicted airloads. The blade-tip sectional airloads are dependent on the nozzle flow conditions, thus requiring an iterative procedure. An initial run of each collective pitch angle is performed using the tip-jet-ejector airload data from the final sizing solution at a collective pitch angle of 12 deg. The CFD models recompute the tip-jet-ejector sectional lift and drag using the updated tip-jet-ejector thermodynamic solution for each collective pitch angle. This procedure is repeated iteratively until the relative change in convergence metrics is below the specified threshold.

There are 168 CFD model cases per iteration for the selected collective-pitch-angle performance sweep. The collective pitch

**Table 6 Rotor thrust and power comparison**

| | Collective, deg | $C_T$ | $C_P$ |
|---|---|---|---|
| Clean rotor | 12.00 | 7.97E − 03 | 8.27E − 04 |
| Tip-jet-ejector rotor | 12.00 | 6.87E − 03 | 8.53E − 04 |
| Tip-jet-ejector rotor | 13.33 | 7.97E − 03 | 1.01E − 03 |
| Constant collective pitch angle, % | —— | −13.80 | 3.14 |
| Constant thrust, % | 9.94 | —— | 17.87 |

**Table 7 Sizing and performance model comparison**

| | Sizing version | Performance version | Difference, % |
|---|---|---|---|
| *Ejector flow parameters* | | | |
| Primary-nozzle mass flow rate, lb/s | 0.31 | 0.31 | −0.47 |
| Upper secondary mass flow rate, lb/s | 0.09 | 0.09 | 0.66 |
| Lower secondary mass flow rate, lb/s | 0.09 | 0.09 | −0.27 |
| Total mass flow rate, lb/s | 0.49 | 0.49 | −0.43 |
| Exit Mach number | 0.70 | 0.70 | −0.50 |
| Exit mean velocity, ft/s | 1165.33 | 1166.87 | −0.13 |
| Exit stagnation temperature, R | 1282.88 | 1279.97 | 0.23 |
| Ejector-nozzle thrust, lb | 21.40 | 21.20 | 0.93 |
| *Rotor and tip-jet parameters* | | | |
| Power required, hp | 18.00 | 17.88 | 0.67 |
| Blade collective pitch angle, deg | 12.00 | 12.00 | —— |
| Fuel flow: jet propellant 8, gal/h | 4.69 | 4.72 | −0.65 |

selected for the sizing procedure is repeated during the performance sweep to check that the performance version of the model matches the sizing version. The accuracy of this match is presented in Table 7. The performance version of the tip-jet-ejector model shows good agreement with the sizing version. The difference between the initial iteration and the final iteration for the range of collective pitch angles is shown in Fig. 23 in terms of the ejector-exhaust-flow total residual. Increasing the number of iterations for the collective-pitch-angle cases will improve the overall convergence. The maximum residual of 3% occurs at the lowest collective pitch angle analyzed. This is a relatively low residual and therefore the computational cost is traded against the increase in model accuracy.

A comparison of the rotor power required and figure of merit as a function of thrust between the tip-jet-ejector rotor and a clean rotor of similar configuration is presented in Figs. 24 and 25, respectively. The tip-jet-ejector rotor shows the expected increase in power and reduction in efficiency due to the added geometry and tip-jet-ejector nozzle flow. Additionally, the rotor thrust is reduced for a given collective pitch angle, indicated by the horizontal shift of the curve to the left, compared with the clean rotor configuration. The amount of fuel used by the tip jet over the range of collective pitch angles is presented in Fig. 26. This trend follows the power curve trend, as expected for a tip-jet-driven rotor. Figure 27 shows a comparison of the mean nozzle exit velocity between the primary nozzle and ejector nozzle computed by the tip-jet-ejector thermodynamic model. There is a significant reduction in the mean ejector-nozzle exit velocity. This reduction will likely result in lower noise generation by the tip-jet ejector nozzle, compared with the tip-jet nozzle alone. The ejector-exit velocity profile will likely have shapes similar to the profiles shown in Fig. 14, in which there is a clear peak in velocity magnitude near the ejector centerline. Using the peak velocity will increase the noise estimation, compared with the mean velocity computed by the thermodynamic model. A prediction of the velocity profile at the exit plane of the ejector nozzle including a forced-

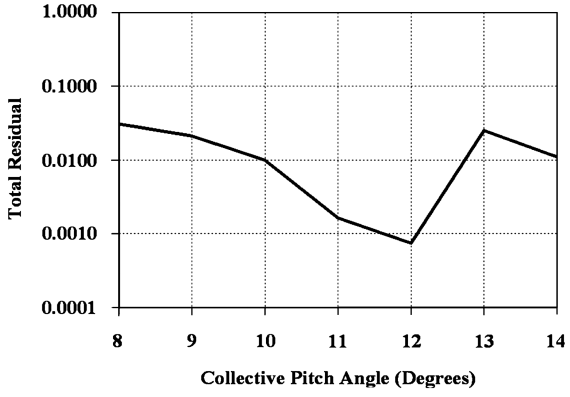


**Fig. 23 Ejector-exhaust-flow total residual.**

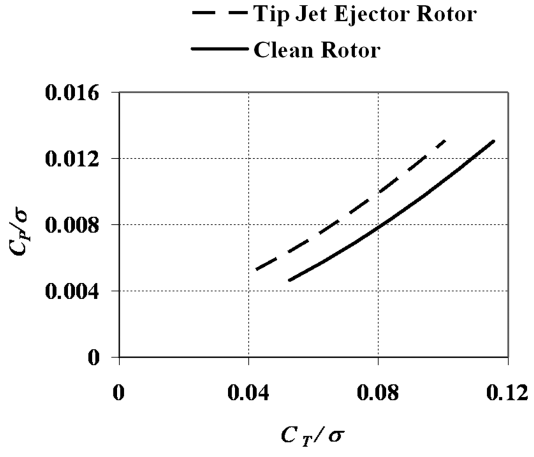


**Fig. 24 Rotor power versus thrust comparison.**

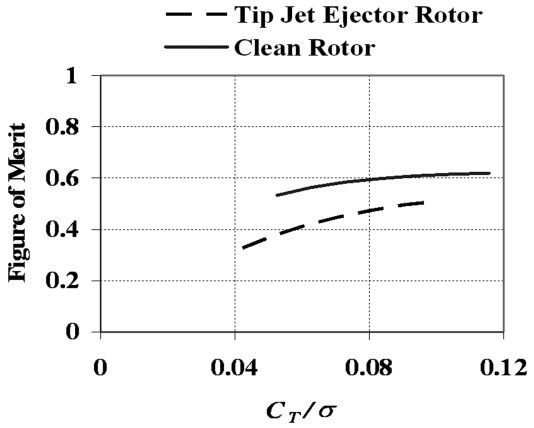


**Fig. 25 Rotor figure of merit versus thrust comparison.**

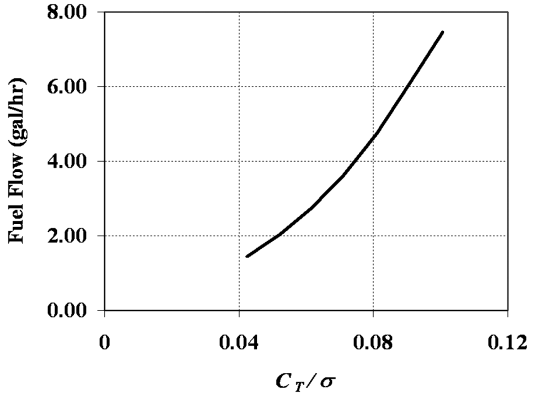


**Fig. 26 Tip-jet fuel flow versus rotor thrust.**

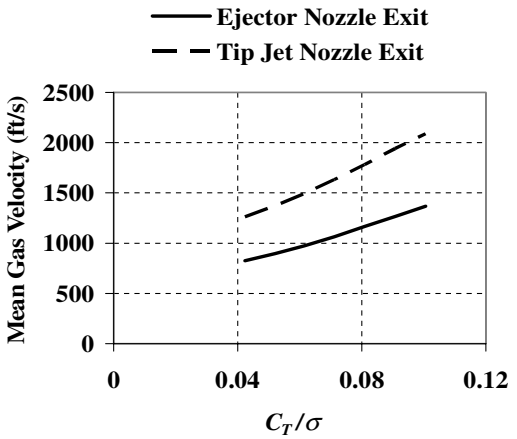


**Fig. 27 Mean nozzle exit velocity versus rotor thrust.**

mixing nozzle requires a three-dimensional CFD model. There are other factors that may contribute to the noise generated by the tip-jet ejector nozzle in addition to the jet noise, including shock-associated noise generated in the supersonic nozzle flow, noise generated by the turbulent mixing of the low-speed secondary and high-speed primary flows, and noise generated by acoustic resonance interactions within the ejector shroud.

## IV. Conclusions

The primary focus of this study identifies the cross-disciplinary coupling and presents an analytical method to address sizing and performance of a tip-jet-ejector-driven rotor. The study also provides some insight into the aerodynamic and thermodynamic characteristics of this tip-jet-ejector rotor configuration in the hovering-flight condition. Although the primary motivation for this study is based on the reduction of the noise generated by a reaction-drive rotor configuration, only the basic aerodynamic and thermodynamic aspects are investigated, with the intent of providing a foundation for both higher-fidelity aerodynamic modeling and acoustic predictions.

It is recognized that not all of the fluid dynamic processes and interactions are captured under the present assumptions. However, the reduced computational modeling effort allows for design tradeoffs and basic performance trends to be performed for this rotor configuration in an early stage of design that may lack detailed knowledge of the rotor. Full integration of the grid generation and CFD modeling into both the sizing and performance procedures will reduce the modeler's effort and the possibility of human error. The solver within the thermodynamic model iteratively solves for the unknowns in the system, requiring reasonable initial values to successfully achieve the solution. Additionally, it was discovered that the amount of fuel burned in the tip jet needed to be increased over the value required by the tip jet alone (without the ejector) for the thermodynamic model to reach a feasible solution. In fact, the percentage of increase in the amount of fuel burned by the tip-jet ejector may be treated as a design variable, due to its influence on the final thermodynamic solution.

Future efforts to improve the utility of this analytical process include adding forward-flight capability and acoustic model coupling to address the potential noise-reduction benefits for a broad range of flight conditions. Additionally, three-dimensional modeling of a hovering rotor with a tip-jet ejector nozzle will remove some of the assumptions, providing a more detailed analysis of the flow interactions at the blade-tip region.

## References

[1] Prouty, R. W., "Performance Analysis," *Helicopter Performance, Stability, and Control*, Krieger, Malabar, FL, 1986, pp. 344–345.

[2] Leishman, J. G., "Conceptual Design of Helicopters," *Principles of Helicopter Aerodynamics*, Cambridge Univ. Press, New York, 2000, pp. 199–201.

[3] Stepan, A., "The Pressure Jet Helicopter," *Journal of the Royal Aeronautical Society*, Vol. 62, Feb. 1958, pp. 123–131.

[4] Nichols, J. B., "The Pressure-Jet Helicopter Propulsion System," Hughes Tool Co., Aircraft Div., Rept. 70-81, Mesa, AZ, 1970.

[5] Harned, M. S., Amer, K. B., and Sullivan, R. J., "Hot Cycle Rotor/Wing for high-speed City Transportation," 4th Annual Meeting and Technical Display, AIAA Paper 67-770, Anaheim, CA, Oct. 1967.

[6] Phillips, J. D., "An Efficient Tip Jet Drive," Aircraft Design Systems and Operations Meeting, AIAA Paper 91-3124, Baltimore, MD, Sept. 1991.

[7] Lighthill, M. J., "On Sound Generated Aerodynamically: I. General Theory," *Proceedings of the Royal Society of London, Series A: Mathematical and Physical Sciences*, Vol. 211, No. 1107, Mar. 1952, pp. 564–587. doi:10.1098/rspa.1952.0060

[8] Porter, J. L., and Squyers, R. A., "A Summary/Overview of Ejector Augmenter Theory and Performance," Vought Corp. Advanced Technology Center, Rept. R-91100/9CR-47A, Dallas, TX, 1979.

[9] Presz, W. Jr., Reynolds, G., and Hunter, C., "Thrust Augmentation with Mixer/Ejector Systems," 40th AIAA Aerospace Sciences Meeting and Exhibit, AIAA Paper 2002-0230, Reno, NV, Jan. 2002.

[10] Loka, M., Robichaud, M., Di Bartolomeo, W., Loe, D., and Sowers, D., "Aerodynamic Optimization of the Exhaust-Ejector on the Tiltrotor Using Navier–Stokes Analysis," 40th AIAA Aerospace Sciences Meeting and Exhibit, AIAA Paper 2000-0986, Reno, NV, Jan. 2000.

[11] Presz, W., Jr., Paterson, R., and Werle, M., "Fluid Dynamic Pump," U.S. Patent No. 4,835,961, 6 June 1989.

[12] Lord, W. K., Jones, C. W., Stern, A. M., Head, V. L., and Krejsa, E. A., "Mixer Ejector Nozzle for Jet Noise Suppression," 26th Joint Propulsion Conference, AIAA Paper 90-1909, Orlando, FL, July 1990.

[13] Landgrebe, A. J., "An Analytical and Experimental Investigation of Helicopter Rotor Performance and Wake Geometry Characteristics," U.S. Army, USAAMRDL-TR-71-24, 1971.

[14] Landgrebe, A. J., "The Wake Geometry of a Hovering Rotor and Its Influence on Rotor Performance," *Journal of the American Helicopter Society*, Vol. 17, No. 4, 1972, pp. 2–15.

[15] Stepniewski, W. Z., and Keys, C. N., "Vortex Theory," *Rotary-Wing Aerodynamics*, Dover, New York, 1984, p. 146.

[16] Spence, D. A., "The Lift Coefficient of a Thin, Jet-Flapped Wing," *Proceedings of the Royal Society of London, Series A: Mathematical and Physical Sciences*, Vol. 238, No. 1212, Dec. 1956, pp. 46–68. doi:10.1098/rspa.1956.0203

[17] Ives, D. C., and Melnik, R. E., "Numerical Calculation of the Compressible Flow over an Airfoil with a Jet Flap," 7th AIAA Fluid and Plasma Dynamics Conference, AIAA Paper 74-542. Palo Alto, CA, June 1974.

[18] Dippold, V. F., III., "Numerical Assessment of the Performance of Jet-Wing Distributed Propulsion on Blended-Wing-Body Aircraft," M.S. Thesis, Virginia Polytechnic Inst. and State Univ., Blacksburg, VA, July 2003.

[19] Henry, J. R., "One Dimensional, Compressible, Viscous Flow Relations Applicable to Flow in a Ducted Helicopter Blade," NACA TN 3089, Oct. 1953.

[20] Hall, David W., "A Compact Methodology for Estimating Duct Losses in Subsonic Inlets," NASA Ames Research Center, Moffett Field, CA, Jan. 1995.

[21] Tai, Jimmy C. M., "A Multidisciplinary Design Approach to Size Stopped Rotor/Wing Configurations Using Reaction Drive and Circulation Control," Ph.D. Thesis, Georgia Inst. of Technology, Atlanta, Aug. 1998.

[22] Fox, R. W., and McDonald, A. T., "Internal Incompressible Viscous Flow," *Introduction to Fluid Mechanics*, 5th ed., Wiley, New York, 1998, pp. 357–368.

[23] Moody, L. F., "Friction Factors for Pipe Flow," *Transactions of the ASME*, Vol. 66, No. 8, Nov. 1944, pp. 671–684.

[24] Nordstrom, K. E., Marsh, A. H., and Sargisson, D. F., "Conceptual Design of Advance Acoustic-Composite Nacelles," NASA CR-132703, July 1975.

[25] Krist, S. L., Biedron, R. T., and Rumsey, C. L., "CFL3D User's Manual (Ver. 5.0)," NASA TM-1998-208444, June 1998.

[26] Steinbrenner, J., Wyman, N., and John Chawner, "Fast Surface Meshing on Imperfect CAD Models," *Proceedings of the 9th International Meshing Roundtable*, Sandia National Labs. Rept. SAND 2000-2207, Albuquerque, NM, 2–5 Oct. 2000, pp. 33–41.

[27] John Chawner, Steinbrenner, J., and Wyman, N., "Hybrid Grid Generation for Complex Geometries Using Gridgen," *Proceedings from the 7th International Conference on Numerical Grid Generation in Computational Field Simulations*, Mississippi State Univ., Mississippi State, MS, Sept. 2000, pp. 417–426.

[28] Richardson, L. F., "The Approximate Arithmetical Solution by Finite

Differences of Physical Problems Including Differential Equations, with an Application to the Stresses in a Masonry Dam," *Philosophical Transactions of the Royal Society of London*, Series A 210, 1910, pp. 307–357.

[29] Roache, P. J., *Verification and Validation in Computational Science and Engineering*, Hermosa, Albuquerque, NM, 1998.

[30] Caradonna, F. X., and Tung, C., "Experimental and Analytical Studies of a Model Helicopter Rotor in Hover," NASA TM 81232, Sept. 1981.

[31] Tung, C., Pucci, S. L., Caradonna, F. X., and Morse, H. A., "The Structure of Trailing Vortices Generated by Model Rotor Blades," NASA TM 81316, Aug. 1981.

[32] Gilbert, G. B., and Hill, P., "Analysis and Testing of Two-Dimensional Slot Nozzle Ejectors with Variable Area Mixing Sections," NASA CR-2251, May 1973.

[33] Dadone, L. U., "U.S. Helicopter Design Datcom Volume 1—Airfoils," Boeing Vertol Co., Rept. D210-11097-1, Philadelphia, May 1976.

[34] Clark, R. L., "Ejector Blown Lift/Cruise Flap Wind Tunnel Investigation," Air Force Flight Dynamics Lab., Rept. AD-777181, Wright-Patterson AFB, OH, Nov. 1973.